



HAL
open science

Algorithmic adjustment of neural field parameters

Frédéric Alexandre, Jérémy Fix, Nicolas P. Rougier, Thierry Viéville

► **To cite this version:**

Frédéric Alexandre, Jérémy Fix, Nicolas P. Rougier, Thierry Viéville. Algorithmic adjustment of neural field parameters. [Research Report] RR-6923, INRIA. 2009, pp.26. <inria-00382533>

HAL Id: inria-00382533

<https://inria.hal.science/inria-00382533v1>

Submitted on 8 May 2009

HAL is a multi-disciplinary open access archive for the deposit and dissemination of scientific research documents, whether they are published or not. The documents may come from teaching and research institutions in France or abroad, or from public or private research centers.

L'archive ouverte pluridisciplinaire HAL, est destinée au dépôt et à la diffusion de documents scientifiques de niveau recherche, publiés ou non, émanant des établissements d'enseignement et de recherche français ou étrangers, des laboratoires publics ou privés.



HAL Authorization

Algorithmic adjustment of neural field parameters

Frédéric Alexandre, Jérémy Fix, Nicolas Rougier, Thierry Viéville

N° 6923

Mai 2009

Thème BIO



*Rapport
de recherche*

Algorithmic adjustment of neural field parameters

Frédéric Alexandre*, Jérémy Fix*, Nicolas Rougier*, Thierry Viéville*

Thème BIO — Systèmes biologiques
Équipes-Projets Cortex

Rapport de recherche n° 6923 — Mai 2009 — 26 pages

Abstract: Revisiting neural-field calculation maps in the discrete case, we propose algorithmic mechanisms allowing to choose a right set of parameters in order to both (i) guaranty the stability of the calculation and (ii) tune the shape of the output map.

These results do not “prove” the existence of stable bump solutions, this being already known and extensively verified numerically, but allow to calculate algorithmically the related parameters.

The results apply to scalar and vectorial neural-fields thus allowing to bypass the inherent limitations brought by mean frequency models and also take the laminar structure of the cortex or high-level representation of cortical computations into account.

We obtain an easy to implement procedure that guaranty the convergence of the map onto a fixed point, even with large sampling steps. Furthermore, we report how rectification is the minimal required non-linearity to obtain usual neural-field behaviors. We also propose a way to control and tune these behaviors (filtering, selection, tracking, remanence) and optimize the convergence rate.

This applies to both non parametric profiles, i.e. adjusting the weight values directly, or to parametric profiles and thus adjusting their parameters (e.g. Mexican-hat profiles).

Beyond these algorithmic results, the idea of studying neural computations as discrete dynamical systems and not only the discretization of a continuous system is emphasized here.

The outcome is shared as an open-source plug-in module, called EnaS (<http://enas.gforge.inria.fr>), to be used in existing simulation software.

Key-words: Discrete neural fields, meta-parameters.

* INRIA Cortex <http://cortex.loria.fr>

Ajustement algorithmique des paramètres de champ neuronaux

Résumé : Le calcul de cartes de champ neuronaux est revisité dans le cas discret et un mécanisme algorithmique pour choisir l'ensemble des paramètres est proposé afin de (i) garantir la stabilité des calculs et (ii) ajuster la forme de la carte de sortie.

Ces résultats ne prouvent pas l'existence des solutions en forme de bulle, ceci ayant déjà été montré par ailleurs, mais permettent de calculer de manière algorithmique les paramètres idoines.

Les résultats s'appliquent au cas scalaire et vectoriel, donc permettent d'aller au delà des modèles qui ne prennent en compte que la fréquence de décharge, et permettent de prendre en compte la structure laminaire du cortex ou des représentations plus abstraites des calculs corticaux.

Nous obtenons une procédure facile à implémenter, avec une convergence de la carte vers un point fixe garantie, au delà du schéma classique d'Euler, optimisant la vitesse de convergence. Nous montrons aussi qu'une non-linéarité limitée à une rectification suffit à simuler les comportements usuels des champs neuronaux, tandis que nous décrivons comment en ajuster les comportements de filtrage, sélection, poursuite et rémanence.

Ceci s'applique à la fois aux mécanismes non-paramétriques (ajustement des valeurs des poids) et paramétriques (ajustement des paramètres d'un profil prédéfini).

Cela montre aussi l'intérêt de travailler directement sur des systèmes discrets de champs neuronaux plutôt que sur la discrétisation de systèmes continus.

Le résultat de ce travail est disponible sous la forme d'un module logiciel "open-source", dit EnaS (<http://enas.gforge.inria.fr>), à utiliser comme "plug-in" dans les logiciels de simulation existants.

Mots-clés : Champs neuronaux discrets, Méta-paramètres

1 Introduction

Using DNF and its extensions. The Dynamic Neural Field (DNF) theory is mainly concerned with the functional modeling of neural structures where information is considered to be encoded at the level of the population rather than at the level of single neurons. Such models first appeared in the 50s, but the theory really took off in the 70s with the works of Wilson and Cowan [27] and Amari [2]. At the level of a single neuron, the model that is used is a mean frequency model, while the electrical activity of a neuron is approximated by a single potential. However, there also exists several spiking neuron models that represent both a finer and more accurate model of a real biological neuron. In the framework of the DNF, such models allow to bypass the inherent limitations brought by mean frequency models [22], this being taken into account via vectorial neural state [25]. Furthermore, neural-fields also allow to consider high-level representation of cortical computations [24].

These models most generally use excitatory recurrent collateral connections between the neurons as a function of the distance between them and global inhibition is used to ensure the uniqueness of the bubble of activity within the field [21]. They exhibit so-called bump patterns, which have been observed in the prefrontal cortex and are involved in working memory tasks [11] or high-level cognition [23].

The dynamics of pattern formation in lateral-inhibition type neural fields with global or local inhibition has been extensively studied in a number of works where it has been demonstrated that these kinds of fields are able to maintain a localized packet of neuronal activity that can, for example, represent the current state of an agent in a continuous space or reflect some sensory input feeding the field [21]. A step further, the linear response of neural fields to localized inputs subject to finite propagation speeds has been studied in [17]. The characteristic behavior of such fields is the formation of very localized packets of neural activity that tend to represent some consistent information which is present at the level of the input [13].

However, the exact shape of these output bumps is quite difficult to predict since it is a generally a non linear consequence of both the lateral connectivity pattern and the input pattern. Thus the question remains on how to control the shape, first in a purely mechanical way (i.e. finding the proper mathematics behind), second in a more biological plausible way. This second step, which is beyond the scope of this paper, requires to complete the first step, which is also going to provide some description of the space of interesting parameters.

The main computational properties (see e.g., [21] for a review) of such neural field are:

- . -1- filtering of the output bump shape: increase versus decrease of size, volume, etc..
- . -2- selection of the output bump among several input bumps,
- . -3- tracking of a moving input bump at the output level,
- . -4- remanence of the output bump after the partial or total suppression of the input bump.

We are going to consider filtering and selection behaviors in this contribution and discuss the tracking and remanence mechanisms also.

The parameter adjustment problem. Here, we want to study which set of lateral weights allow to achieve a specific function, and obtain one unique controlled bump on the output. More precisely, the goal of this paper is to provide algorithmic results to

this parameter adjustment problem. This contrasts with the almost universal practice to adjust empirically the parameters of neural field (even if authors are unobtrusive about it), although constructive results exist and should be used.

In [13], for instance, homogeneous stationary solutions (i.e independent of the spatial variable) and bump stationary solutions (i.e. localized areas of high activity) in two-dimensional neural field models composed of excitatory and inhibitory neurons have been studied, in the continuous case, after [6, 9], providing an explicit solution in terms of Bessel functions and Hankel transform. Basic properties of bounded neural fields (well-posedness, stability of their solutions in the homogeneous or locally homogeneous case) have also been studied, accounting for partial or global synchrony among the cortical columns composing the field [14]. These results are based on the compactness of the related operators yielding stability results related to contracting mappings.

These results however are not easy to implement in practical codes, because, in order to obtain analytical results they consider formulations (using e.g. Heaviside non-linearity and/or unlimited precision assumptions) which do not correspond to numerical implementations. Furthermore, in the discrete case, we may obtain more interesting results than simply approximating using “small- ϵ ” results obtained in the continuous case. This means not simply consider the Euler approximation of the continuous equation but also consider more efficient discrete schemes. This also means not derive parameter adjustment algorithmic mechanisms based on approximations of continuous solutions, but build on the discrete solution directly.

What is the paper about. In the next section we review the formalism usually considered for neural field implementation. We discuss the choice of the output-state non linear relation and the way bumps are defined. We also make explicit one link between the continuous and discretized approaches.

In the first result section, we derive a sufficient condition to guaranty the convergence of the neural map towards a fixed point, given the proposed non-linearity, and discuss its applications.

In the next result section, we introduce a linear framework to define the optimal neural field weights given an input-output relation. We instantiate this mechanism for parametrized weights and local bounded weights.

In the conclusion we briefly discuss the limits and applications of the methods proposed here.

2 Methods

Defining a continuous map.

Let us consider¹ a dynamic *vectorial* map $\mathbf{v} : \mathcal{S}^n \times \mathcal{R} \rightarrow \mathcal{R}^m$ (e.g., for a 2D scalar map $n = 2, m = 1$) defined from:

$$\begin{cases} \tau \dot{\mathbf{v}}(\mathbf{x}, t) &= -\mathbf{L} \mathbf{v}(\mathbf{x}, t) + \int_{\mathbf{y}} \mathbf{W}(\mathbf{x} - \mathbf{y}) \mathbf{a}(\mathbf{y}, t) d\mathbf{y} + \mathbf{G} \mathbf{i}(\mathbf{x}), \\ \mathbf{a}(\mathbf{x}, t) &= \rho(\mathbf{v}(\mathbf{y}, t)), \\ \mathbf{v}(\mathbf{x}, 0) &= \mathbf{G} \mathbf{i}(\mathbf{x}), \end{cases} \quad (1)$$

¹*Notations:* Scalar are written in italic, vectors are written with lower-case bold letters and matrices with upper-case bold letters. The identity matrix is written \mathbf{I} . For a scalar function $f()$ applied to a vector \mathbf{u} , $\mathbf{v} = f(\mathbf{u})$ means $\forall i, v_i = f(u_i)$.

where at location \mathbf{x} and time t , $\mathbf{v}(\mathbf{x}, t)$ represents the unit *state* (related to the membrane potential in scalar models) and $\mathbf{a}(\mathbf{x}, t)$ accounts for the unit output positive *activity* (usually related to the firing rates in scalar models).

Here, $\mathbf{i}(\mathbf{x})$ models the input (related to a membrane current in scalar models). It is supposed constant in the sequel, unless explicitly specified (i.e. when considering tracking and remanence).

The spatial domain of the model is a hyper-sphere \mathcal{S}^n though the domain is assumed to be large enough to neglect boundary conditions. Numerical verifications are going to validate this approximation.

Here, we do not consider only a scalar map but also a vectorial map in order to take more complex neural models (e.g., [22]) or several cortical layer (see [12] for an illustration) or more complicated functional mechanisms (see [24] for a discussion) into account.

For the input gain \mathbf{G} , we assume without loss of generality $\mathbf{G} = \mathbf{I}$ in the sequel (i.e. considering the $\mathbf{G} \mathbf{i} \rightarrow \mathbf{i}$ transform).

Similarly, for the diagonal matrix $\mathbf{L} \geq 0$ (i.e. a positive matrix, thus with positive diagonal elements) which accounts for the neural unit leak, without loss of generality (i.e. considering the $\mathbf{v} \rightarrow \sqrt{\mathbf{L}}^{-1} \mathbf{v}$ transform), we assume $\mathbf{L} = \mathbf{I}$ in the sequel.

The matrix \mathbf{L} is diagonal, but in the vectorial case, the interactions between layers, i.e. between the components of \mathbf{v} , are defined via the non-diagonal elements of the $\mathbf{W}(\mathbf{d})$ matrices.

The map is parametrized by the recurrent connection weights \mathbf{W} . One example are radial ‘‘Mexican hat’’ connections (i.e. with exponential excitatory/inhibitory connections) which writes in the scalar case:

$$W_\phi(\mathbf{y}) = \mathbf{A}_+ e^{-|\mathbf{y}|^2/\sigma_+} - \mathbf{A}_- e^{-|\mathbf{y}|^2/\sigma_-},$$

parametrized by $\phi = (A_+, A_-, \sigma_+, \sigma_-)$, accounting for the excitatory and inhibitory gains and geometries, respectively. Other parametric instances are also considered in the present framework.

In any case, the goal is to tune the weights \mathbf{W} in order to control the map’s output. This shall be done either by nonparametric profiles, i.e. thus adjusting the weight values \mathbf{W} directly, or by parametric profiles and thus adjusting their parameters ϕ .

Defining the output-state relation.

In this context, the output-state relation is modeled as a point-like non-linearity, as illustrated in Fig. 1.

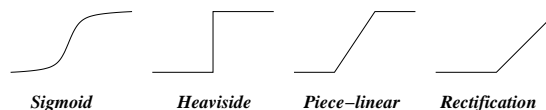


Figure 1: Schematic representation of usual output-state non-linear relations in neural field equations: The sigmoid profile corresponds to the average relation between membrane potential and firing rate. The binary Heaviside profile is considered in order to ease analytical derivations. The piece-wise linear profile allows to take thresholding and saturation into account in conjunction with a linear response. The rectification profile takes into account the fact that the neural activity is constrained to positive values. In this contribution, we consider rectification and, to some extends, piece-linear profiles.

The sigmoid profile corresponds to the average relation between membrane potential and firing rate (assuming slow variation of the potential with respect to firing-rate sampling measure and Gaussian distributions of membrane potential and firing threshold, see e.g., [7] for a review) and it is very often simplified as a piece-wise linear profile (thus with thresholding and saturation bounding a linear response) or even a drastic Heaviside profile used for analytical derivation purposes (e.g., [12]). The reason for this over-simplification is the need to derive analytical results with the caveat to model the input activity down to a simple on-off process, though analytical studies considering the sigmoidal shape of the transfer function are also available [8, 4]. Another choice is to accept the fact that, up to our current knowledge, the level of modelization of a neural field is rather far from the biological complexity. Applying the Occam razor principle, the fact that the neural activity, viewed as a firing-rate, is thus constrained to positive values can be considered as the minimal assumption related to biological constraints (see, e.g. [15] for an early contribution and a deep discussion on the subject). This minimal choice also results from the following numerical fact: It has been observed that (see e.g. Fig.2), with “suitable” parameters, interesting properties of neural fields (filtering, selection, tracking) [20, 21] can be obtained using rectification (instead of usual sigmoid-like profiles).

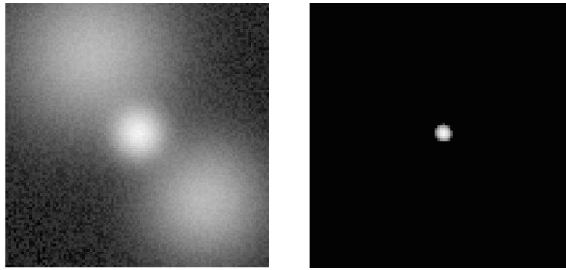


Figure 2: An example of input (*left-view*) output (*right-view*) transformation via a non-linear discrete map with rectification. The input is noisy (more than 20% of the signal) with three bumps. The output “filters” the noise, and select the highest bump even if the lower bumps have more energy (being wider). This result is obtained, from (2) with Mexican-Hat profiles $\phi = (0.0015, 0.0015, 0.45 N, N)$, $N = 100$ and $\delta = 0.99$. Furthermore, with the same parameters, if the bump is moving, the mechanism tracks the highest bump.

We thus are going to consider rectification as output-state relation in the sequel. We are also going to explain how the following results still apply to piece-wise linear sigmoid-like profiles.

Using a numeric non-linear discrete map.

Since we want to derive algorithmic results, we must make explicit the numeric implementation of the previous theoretic equations.

Let us thus consider the following non-linear synchronous discrete scheme in time and space, thus, now² for $\mathbf{x} \in \{0, N\}^n$ and $t \in \{0, T\}$, $T < +\infty$:

$$\begin{aligned} \mathbf{u}^+(\mathbf{x}, t) &= \rho(\mathbf{u}(\mathbf{x}, t)), \\ \mathbf{u}(\mathbf{x}, t+1) &= \mathbf{u}^+(\mathbf{x}, t) + \delta \left(-\mathbf{u}^+(\mathbf{x}, t) + \sum_{\mathbf{y}} \mathbf{W}(\mathbf{x} - \mathbf{y}) \mathbf{u}^+(\mathbf{y}, t) + \mathbf{i}(\mathbf{x}) \right), \\ \mathbf{u}^+(\mathbf{x}, 0) &= \mathbf{i}(\mathbf{x}), \end{aligned} \tag{2}$$

providing $0 < \delta < 1$, while³ the non-linearity $\rho(\cdot)$ is a rectification, thus with $\mathbf{u}^+(\mathbf{x}, t) \geq 0$.

This writes in compact matrix form:

$$\begin{aligned} \bar{\mathbf{u}}^+(t+1) &= \mathbf{F}(\bar{\mathbf{u}}^+(t)) \\ &= \rho(\bar{\mathbf{u}}^+(t) + \delta [-\bar{\mathbf{u}}^+(t) + \bar{\mathbf{W}} \cdot \bar{\mathbf{u}}^+(t) + \bar{\mathbf{i}}]) \\ &= \rho(\bar{\mathbf{K}} \bar{\mathbf{u}}^+(t) + \delta \bar{\mathbf{i}}), \quad \bar{\mathbf{K}} = 1 - \delta [1 - \bar{\mathbf{W}}], \end{aligned}$$

where $\bar{\mathbf{u}}^+$ is a $\mathcal{R}^{n \times m}$ vector, while $\bar{\mathbf{W}}$ and $\bar{\mathbf{K}}$ are $\mathcal{R}^{(n \times m) \times (n \times m)}$ Toeplitz matrices.

This corresponds to what is implemented in simulation codes (e.g., [20, 21]). However, the link between (1) (with $\mathbf{K} = \mathbf{L} = \mathbf{I}$) and (2) is not straightforward and has to be carefully derived, as performed now.

The derivation is not straightforward because (2) is not the Euler discretization scheme of (1). This latter scheme writes:

$$\begin{aligned} \mathbf{u}(\mathbf{x}, t+1) &= \mathbf{u}(\mathbf{x}, t) + \Delta T \dot{\mathbf{u}}(\mathbf{x}, t) \\ &= \mathbf{u}(\mathbf{x}, t) + \delta \left(-\mathbf{u}(\mathbf{x}, t) + \sum_{\mathbf{y}} \mathbf{W}(\mathbf{x} - \mathbf{y}) \mathbf{u}^+(\mathbf{y}, t) + \mathbf{i}(\mathbf{x}) \right) \end{aligned} \tag{3}$$

for a sampling period ΔT , with $\delta = \Delta T / \tau$ and providing $\mathbf{u} \stackrel{\text{def}}{=} \mathbf{v}$ and $\mathbf{u}^+ \stackrel{\text{def}}{=} \mathbf{a}$.

If $\mathbf{v}(\mathbf{x}, t) > 0$, \mathbf{v} being differentiable (thus continuous), then in a neighborhood $s \in]t - \epsilon, t + \epsilon[$ $\mathbf{v}(\mathbf{x}, s) > 0$, thus $\mathbf{u}(\mathbf{x}, s) = \mathbf{u}^+(\mathbf{x}, s)$ and $\dot{\mathbf{u}}(\mathbf{x}, s) = \dot{\mathbf{v}}(\mathbf{x}, s)$ so that both schemes correspond, because (1) and (2) behave as linear equations.

Otherwise, if $-\mathbf{v}(\mathbf{x}, t) \geq 0$ then for identical $\mathbf{u}(\mathbf{x}, t)$ and $\mathbf{u}^+(\mathbf{x}, t) = 0$ schemes (2) and (3) verify:

$$\begin{aligned} \delta (\tau \dot{\mathbf{v}}(\mathbf{x}, t) + \mathbf{v}(\mathbf{x}, t)) &= \\ \mathbf{u}(\mathbf{x}, t+1)|_{(3)} + (1 - \delta)(-\mathbf{v}(\mathbf{x}, t)) &= \mathbf{u}(\mathbf{x}, t+1)|_{(2)} \geq \mathbf{u}(\mathbf{x}, t+1)|_{(3)} \end{aligned}$$

so that:

If $\mathbf{v}(\mathbf{x}, t) \leq 0$ and $\tau \dot{\mathbf{v}}(\mathbf{x}, t) \leq -\mathbf{v}(\mathbf{x}, t)$ both schemes still correspond, since

$$0 \geq \mathbf{u}(\mathbf{x}, t+1)|_{(2)} \geq \mathbf{u}(\mathbf{x}, t+1)|_{(3)} \Rightarrow \mathbf{u}(\mathbf{x}, t+1)^+|_{(2)} = \mathbf{u}(\mathbf{x}, t+1)^+|_{(3)} = 0.$$

This conditions occurs if $\dot{\mathbf{v}}(\mathbf{x}, t)$ is small enough, in particular in a neighborhood of fixed points.

As a consequence, if both schemes converge towards a fixed point, the fixed point is the same (same kind and same value).

However if $\mathbf{v}(\mathbf{x}, t) \leq 0$ and $\tau \dot{\mathbf{v}}(\mathbf{x}, t) > \mathbf{v}(\mathbf{x}, t)$ both schemes differ, in the same way the Gauss-Seidel scheme differs from (improving it) the Jacobi scheme for iterative solutions of linear systems. Here the scheme (2) make use of the \mathbf{u}^+ rectified values as soon as available, instead of still using the non rectified values as for the scheme (3). See [18] for a technical development and elements showing the interest⁴ of the ‘‘Gauss-Seidel-like’’ scheme (2) with respect to the ‘‘Jacobi-like’’ scheme (3).

As a conclusion on this aspect, the series (2) converges to a discrete approximation of (1) corresponding to the Euler discretization scheme, the standard numerical scheme being improved here.

Anyway, it is easy to verify that the derivations proposed in the sequel are obvious to adapt to the scheme (3), if used instead of the scheme (2).

²We write $\{a, b\} = \{n \in \mathcal{N}, a \leq n < b\}$.

³Here we write $\forall i \in \{1, m\}, \mathbf{u}_i^+ \geq 0$ as $\mathbf{u}^+ \geq 0$ and $\forall i \in \{1, m\}, \mathbf{u}_i^+ = \rho(\mathbf{u}_i)$ as $\mathbf{u}^+ = \rho(\mathbf{u})$. Furthermore:

$$\rho(u) = \max(0, u) = (\text{if } u \geq 0 \text{ then } u \text{ else } 0) = \lim_{\epsilon \rightarrow 0} \rho_\epsilon(u)$$

with $\rho_\epsilon(u) \stackrel{\text{def}}{=} H(u) u e^{-\epsilon/u}$, $H(\cdot)$ being the Heaviside function, are equivalent definitions of a rectification. The $\rho_\epsilon(\cdot)$ function is the \mathcal{C}^∞ mollified form of the rectification.

⁴Interesting enough is the fact that some co-authors of the paper use this scheme for years thanks to their ‘‘computer-scientist’’ intuition, before the following discussion has been made explicit thanks to the ‘‘physicist’’ of the group.

Bump as required output.

In this context, the desired output profile is a bump, i.e. a bell-like profile, more precisely a *positive, decreasing, radial symmetric profile*, as observed for bubble of activities in the cortex [2, 11]. A Gaussian profile is one example of a bump. In order to capture the notion of bump at a more general level, we have proposed to consider Gaussian enumerable linear combinations [1], which is suitable in the linear case, but does not appear to be easily translatable to the non-linear case.

Following another track, we write a radial symmetric profile (without loss of generality around $\mathbf{x}_0 = \mathbf{0}$) as:

$$\mathbf{u}(\mathbf{x}) = \mathbf{u}(r^2), r = |\mathbf{x}|$$

with $\mathbf{u}(r) > 0$ (positivity) and $\dot{\mathbf{u}}(r) \leq 0$ (decrease).

We further notice that the convolution:

$$(\mathbf{W} * \mathbf{u})(|\mathbf{x}|^2) = \int_{\mathbf{y}} \mathbf{W}(|\mathbf{x} - \mathbf{y}|^2) \mathbf{u}(|\mathbf{y}|^2) d\mathbf{y}$$

of two radial symmetric functions is radial symmetric (easily shown, for instance, considering the invariance by a rotation \mathbf{R} of $(\mathbf{W} * \mathbf{u})(|\mathbf{R}\mathbf{x}|^2) = (\mathbf{W} * \mathbf{u})(|\mathbf{x}|^2)$) while in the general case, $\mathbf{W}(\mathbf{x})$ must be radial symmetric in order the convolution to preserve radial symmetry for any radial function \mathbf{u} . We thus are going to consider radial symmetric weights in the present study, thus only function on the magnitude r .

There is however a tricky point here: *convolution of radial symmetric functions are not magnitude convolutions*. More precisely, in the 2D scalar case⁵:

$$(W * u)(r = |\mathbf{x}|) = \int_s W(s, r) u(s = |\mathbf{y}|) ds$$

with $W(s, r) = s \int_{\theta} W\left(\sqrt{|r - s|^2 + 2rs(1 - \cos(\theta))}\right) d\theta$, whereas, for a convolution, an expression of the form $W(s - r)$ would have been expected.

This misleading fact is overcome in the second next section where a constructive method is proposed to control the bump radial symmetric profiles.

3 Results about the convergence

Let us first discuss how to control the discrete implementation convergence.

Implementation as a contracting mapping.

In order to obtain the convergence of the iterative equation (2) towards a fixed point we simply require the related mapping to be contracting, i.e.

$$\left| \frac{\partial \mathbf{F}}{\partial \mathbf{u}} \right| = |\Sigma' \bar{\mathbf{K}}| < 1$$

where $\Sigma' = \text{diag}(\dots, \rho'_i, \dots)$ is the diagonal matrix with $\rho'_i = \rho'(\bar{\mathbf{K}} \bar{\mathbf{u}}(t) + \delta \bar{\mathbf{i}}) \in \{0, 1\}$ whether the value is negative or positive, respectively.

This allows to write pragmatic conditions of convergence, as discussed now.

This also restrains our study to convergence to a fixed point, without taking other asymptotic dynamics into account [6].

⁵The same results indeed occurs in the n-dimensional vectorial case: $\mathbf{v}(r) = \int_s \mathbf{W}(s, r) \mathbf{u}(s)$ with:

$$\mathbf{W}(s, r) = s^{n-1} \int_{\mathbf{n}} d_{\mu} \mathbf{n} \mathbf{W}\left(\sqrt{|r - s|^2 + 2rs(1 - \mathbf{e}_1^T \mathbf{n})}\right), \mathbf{e}_1 = (1, 0 \dots 0)^T,$$

writing $\mathbf{x} = r \mathbf{m}$, $|\mathbf{m}| = 1$ and $\mathbf{y} = s \mathbf{n}$, $|\mathbf{n}| = 1$ with $d\mathbf{y} = s^{n-1} ds d_{\mu} \mathbf{n}$, and $d_{\mu} \mathbf{n} = \frac{d\mathbf{n}^{\{\dots j \dots\}, j \neq i}}{n^i}$, while $ds = \mathbf{n}^T d\mathbf{y}$, thus not of the form $\mathbf{W}(s - r)$, because of the sr term in the previous expression.

Convergence in the linear case.

Assume that all output values are positive, i.e. $\rho_i = 1$, thus no rectification. This occurs typically with excitatory weights only. This corresponds to a pure linear transformation.

In this case, since $\left| \frac{\partial \mathbf{F}}{\partial \mathbf{u}} \right| = |\bar{\mathbf{K}}|$, the convergence condition now writes:

$$|\bar{\mathbf{K}}| < 1 \Leftrightarrow |\bar{\mathbf{W}}| < 1 \text{ as soon as } 0 < \delta < 1,$$

i.e. in words: the system is contracting if the magnitude of the global weight matrix is lower than one. If higher than one, the system diverges, in the general case.

Since the matrix is symmetric, because we consider radial symmetric weight profiles, its magnitude (defined as $|\bar{\mathbf{W}}| = \max_{\bar{\mathbf{u}}, |\bar{\mathbf{u}}|=1} |\bar{\mathbf{W}} \bar{\mathbf{u}}|$) corresponds to its spectral radius i.e., its eigen-value of highest magnitude.

The previous result is then a consequence of the fact, easy to verify, that $\bar{\mathbf{K}}$ and $\bar{\mathbf{W}}$ have the same eigen-vectors, with corresponding eigen-values $\lambda_{\bar{\mathbf{K}}}$ and $\lambda_{\bar{\mathbf{W}}}$ verifying:

$$\lambda_{\bar{\mathbf{K}}} = 1 - \delta (1 - \lambda_{\bar{\mathbf{W}}}).$$

This condition is simple to check⁶ at the numerical level, using the power method [10], which efficiently calculates the highest matrix eigen-value, i.e., the magnitude of the matrix in our case, via the converging series $(\bar{\mathbf{u}}^s, \lambda^s)$:

$$\begin{cases} \bar{\mathbf{u}}^{s+1} &= \bar{\mathbf{W}} \bar{\mathbf{u}}^s / \lambda^s & \lambda^s = |\bar{\mathbf{u}}^s| \\ \bar{\mathbf{u}}^0 &= (1, \dots, 1)^T & \lambda^0 = |\bar{\mathbf{u}}^0| \end{cases}$$

yielding $|\bar{\mathbf{W}}| = \lambda^\infty$.

We numerically observed that convergence of the previous power-iteration method to estimate $|\bar{\mathbf{W}}|$ up to a precision of 10^{-3} is obtained in about 2 to 5 iterations for the different results reported here, very often 2 to 3, about 10 in the worst cases. This is due to the choice of $\bar{\mathbf{u}}^0$ (never orthogonal to the final eigen-vector, as required by the method) which is close to the final value $\bar{\mathbf{u}}^\infty$. This value has been chosen considering that $\bar{\mathbf{W}}$ is not only a Toeplitz matrix⁷, but close to a circulant matrix (considering the previous boundary conditions), thus with eigen-elements in closed form: This value for $\bar{\mathbf{u}}^0$ corresponds to a eigen-value close to the weight's average value. It is easy to verify, as a rule of thumb, that *the magnitude is always higher than the weight's average value*, while we have numerically observed that both values are closed for high magnitude $|\bar{\mathbf{W}}|$.

Tuning the parameters in the linear case.

The key fact at this point, is that *convergence does not depend on δ* (as soon as lower than 1). It means that we can use high δ values and speed up the convergence. It also means that it is not always an optimal idea to make all the analysis in the continuous case and then blindly “discretize with a small ϵ ”.

More than that, the calculation not only tells if the system is contracting or not, but since the equation is linear, allows to calculate the maximal weight magnitude which guarantees the convergence. In other words, the previous algorithm tells how to *rescale* the gain parameters (e.g., $|\mathbf{A}_-|$ and $|\mathbf{A}_+|$ for Mexican-hat profiles) in order to guaranty the convergence.

Although this is not going to be true in the non-linear case, in the linear case, the final result does not depend on δ and the closed-form solution writes, reintroducing the

⁶Numerical implementations used in this paper are available at <http://enas.gforge.inria.fr>.

⁷The previous condition, although very efficient in practice, does not directly make profit of the fact that $\bar{\mathbf{W}}$ is a Toeplitz matrix. It might however be interesting to explore this algebraic property and analyze to which extends this yields a stronger result about convergence, especially in the non-linear case.

input gain matrix \mathbf{G} defined in (1) for the purpose of the discussion:

$$\bar{\mathbf{u}}(\infty) = [1 - \bar{\mathbf{W}}]^{-1} \bar{\mathbf{G}} \bar{\mathbf{i}}, \quad (4)$$

since $\bar{\mathbf{u}}(t+1) = \bar{\mathbf{K}} \bar{\mathbf{u}}(t) + \delta \bar{\mathbf{G}} \bar{\mathbf{i}}$ in this case, thus:

$$\bar{\mathbf{u}}(\infty) = \sum_t \bar{\mathbf{K}}^t \delta \bar{\mathbf{G}} \bar{\mathbf{i}} = [1 - \bar{\mathbf{K}}]^{-1} \delta \bar{\mathbf{G}} \bar{\mathbf{i}} = [1 - \bar{\mathbf{W}}]^{-1} \bar{\mathbf{G}} \bar{\mathbf{i}}.$$

This formula is instructive because it explains why using a linear map without non-linear output-state relation does not allow the recurrent connections parameterized by $\bar{\mathbf{W}}$ to produce a selection, unless $\bar{\mathbf{G}}$ is singular. The simple reason is that selection means that a whole set of non similar inputs (with the desired bump added to different kind of distractors) map onto the same output (without the distractors). This linear filtering has a kernel reduced to $\{0\}$ thus is not able to project several inputs onto a unique output. If $\bar{\mathbf{G}}$ is singular, selection can be produced, but without any need of the recurrent connections. In fact, in the linear case, the DNF is equivalent to a simple feed-forward filter.

Furthermore, e.g. for scalar Mexican-hat profiles, we can describe how convergence varies with $|A_-|/|A_+|$ and with σ_-/σ_+ , as detailed in Fig. 3.

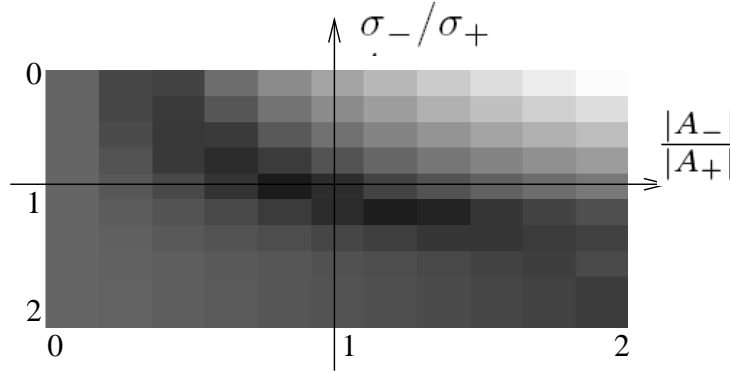


Figure 3: Representation of $|\bar{\mathbf{W}}|$ magnitude variations for Mexican-hat profiles. Here the 2D scalar map size is 100×100 and $\sigma_+ = 10$, while $A_+ = 1/20$, for magnitudes between 0 (black) and 1 (white). Results are obtained in less than 5 iterations of the power-method. We observe the non trivial increase and decrease of the magnitude depending on the inhibitory/excitatory gain and width ratios: It increases with σ_-/σ_+ and decreases with $|A_-|/|A_+|$ when $\sigma_- < \sigma_+$ and $|A_-| < |A_+|$ which corresponds to the intuition that inhibition “balances” excitation. A dual effect is observed when $\sigma_- > \sigma_+$ and $|A_-| > |A_+|$: Inhibition, when not thresholded by the rectification mechanism, also induces high magnitudes, thus instabilities. In other conditions the magnitude is not monotonic.

Using bounded excitation in the non-linear case.

The previous result is quite informative, but does not correspond to our need, since rectification has still to be taken into account. However, we can make use of the previous result and derive the following sufficient boundary condition, in the non-linear case:

$$|\bar{\mathbf{W}}^+| < 1, \quad \bar{\mathbf{W}}^+ = \max(0, \bar{\mathbf{W}}) \quad (5)$$

i.e. in words: *the non-linear solution remains bounded and is convergent if the magnitude of the positive (excitatory) weights is lower than one.*

A few algebra yields, as soon as $\bar{\mathbf{u}} > 0$, i.e., for $t > 0$:

$$\bar{\mathbf{K}} \bar{\mathbf{u}} + \delta \bar{\mathbf{i}} = \underbrace{[1 - \delta [1 - \bar{\mathbf{W}}^+]]}_{\bar{\mathbf{K}}^+} \bar{\mathbf{u}} + \delta \bar{\mathbf{i}} + \underbrace{\delta \min(\bar{\mathbf{W}}, 0)}_{\bar{\mathbf{u}}^<} \bar{\mathbf{u}}$$

with $\bar{\mathbf{u}}^< \leq 0$ and $\bar{\mathbf{u}}^> = \bar{\mathbf{K}}^+ \bar{\mathbf{u}} + \delta \bar{\mathbf{i}} \geq 0$, thus:

$$|\mathbf{F}(\bar{\mathbf{u}}) = \rho(\bar{\mathbf{K}} \bar{\mathbf{u}} + \delta \bar{\mathbf{i}})| \leq |\rho(\bar{\mathbf{K}}^+ \bar{\mathbf{u}} + \delta \bar{\mathbf{i}}) = \bar{\mathbf{K}}^+ \bar{\mathbf{u}} + \delta \bar{\mathbf{i}}|,$$

since $|\rho(\bar{\mathbf{u}}^> + \bar{\mathbf{u}}^<)| \leq |\rho(\bar{\mathbf{u}}^>)|$.

The upper-bounding series defined from:

$$0 \leq \bar{\mathbf{u}}(t+n) \leq \bar{\mathbf{u}}_n^> = (\bar{\mathbf{K}}^+ \bar{\mathbf{u}}_{n-1}^> + \delta \bar{\mathbf{i}}), \bar{\mathbf{u}}_0^> = \bar{\mathbf{u}}(t)$$

is linear and convergent if and only if $|\bar{\mathbf{K}}^+| < 1 \Leftrightarrow |\bar{\mathbf{W}}^+| < 1$, reusing the previous result.

Since $\bar{\mathbf{u}}$ is positive and bounded by a convergent series, it remains bounded (i.e., convergent or oscillatory inside the bounds). However, the previous derivation yields a stronger result because:

$$\forall i, 0 \leq [\Sigma' \bar{\mathbf{K}} \mathbf{u}]_i \leq [\bar{\mathbf{K}}^+ \mathbf{u}]_i$$

since if $[\bar{\mathbf{K}} \mathbf{u}]_i \leq 0 \Rightarrow [\Sigma' \bar{\mathbf{K}} \mathbf{u}]_i = 0$ while $[\bar{\mathbf{K}} \mathbf{u}]_i \leq [\bar{\mathbf{K}}^+ \mathbf{u}]_i$, as derived in the previous lines. Thus

$$\left| \frac{\partial \bar{\mathbf{u}}}{\partial \bar{\mathbf{u}}} \right| = |\Sigma' \bar{\mathbf{K}}| \leq |\bar{\mathbf{K}}| < 1$$

as soon as $|\bar{\mathbf{W}}^+| < 1$ and the series of scheme (2) is contracting as desired.

This captures the intuitive fact that the negative (inhibitory) weights action is always bounded by the rectification, thus only positive weights matter. An example of practical adjustment curve is given in Fig. 4.

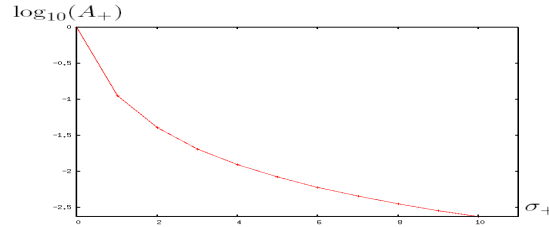


Figure 4: An example of maximal gain curve in the non-linear case. Given σ_+ in abscissa (in pixel unit for a 100×100 2D scalar map), the normalized maximal value of $\log_{10}(A_+)$ is drawn. Here, not a Mexican hat but a step-wise constant profile has been used, in order to illustrate the fact that the derivation can be performed with any kind of weight profile.

Without this condition, as corroborated by numerical experiments, the system is in usual conditions divergent. This is easy to figure out: as soon as an input is closed to the $\bar{\mathbf{W}}^+$ eigen-vector related to the eigen-value higher than one, it is going to induce a divergence, unless the inhibitory weights balance this effect. Since positive excitatory weights are concentrated in a short-range neighborhood, a localized bump essentially activates excitatory connections without inhibition, leading to divergence if $|\bar{\mathbf{W}}^+| \gg 1$. This corresponds to what has been observed numerically, as detailed in Fig. 5. This corresponds to the fact that the proposed condition is sufficient but not necessary. Furthermore, this also does not mean that, given a *restrained* set of inputs, higher parameter's values are not going to yield convergence.

The system is also convergent if $|\bar{\mathbf{W}}| < 1$ but this is a stronger condition which bounds both excitatory / inhibitory connections whereas the proposed condition does not constraint inhibition since the rectification non-linearity allows to stabilize inhibition.

This condition still does not depend on δ , as soon as $\delta < 1$. It does not mean that the way it converges does not depend on δ : Depending on δ the convergence might occur with damped oscillations or not, be either faster or slower, etc.. This has been numerically explored in Fig. 6 leading to a simple rule of thumb to adjust δ .

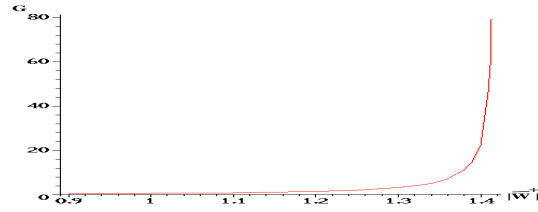


Figure 5: Behavior of the non-linear discrete scheme, when $|\bar{\mathbf{W}}^+| > 1$, for the same experimental conditions as reported in Fig. 2 except that the excitatory weights are reinforced in order to increase $|\bar{\mathbf{W}}^+|$. Given $|\bar{\mathbf{W}}^+|$ in abscissa, the input/output gain G is drawn. We numerically observe the divergence for $|\bar{\mathbf{W}}^+| > \simeq 1.5$. In the intermediate range $|\bar{\mathbf{W}}^+| \in [1.. \simeq 1.5]$ the scheme is still converging to fixed point, but with an exponential gain increase and small residual oscillations observed during the numerical experiment.

$\delta =$	0.01	0.1	0.2	0.3	0.4	0.5	0.6	0.7	0.8	0.9	0.99
$ \mathbf{W}^+ = 0.0$	135	14	5	7	4	6	8	17	$> 10^3$	$> 10^3$	$> 10^3$
$ \mathbf{W}^+ = 0.1$	169	17	9	6	5	5	6	8	14	40	$> 10^3$
$ \mathbf{W}^+ = 0.2$	202	21	11	7	6	5	6	7	10	14	33
$ \mathbf{W}^+ = 0.5$	392	40	21	14	11	9	8	7	7	8	8
$ \mathbf{W}^+ = 0.9$	569	58	30	21	16	13	11	10	9	9	8
$ \mathbf{W}^+ = 0.95$	618	63	33	22	17	14	12	11	10	9	9
$ \mathbf{W}^+ = 0.99$	667	68	35	24	19	15	13	12	10	10	9

Figure 6: Convergence rate measured as the number of iterations to obtain a fixed point up to a mean value variation below 10^{-3} , for the same experimental conditions as reported in Fig. 2 (corresponding to the 1st line of results), except that the excitatory weights are reinforced in order to increase the magnitude (subsequent lines of result). We clearly observed the interest of using non-negligible values of δ , and the influence of the weights magnitude. For small values of the magnitude, a value $\delta \simeq 1/2$ seems optimal with a switch towards $\delta \rightarrow 1$ for highest values of the magnitude. For convergence rate higher than 10^3 the system is mainly oscillating (damped oscillations) while always bounded as predicted.

Application to tracking.

The fact convergence does not depend on δ , as soon as $\delta < 1$, allows to introduce high convergence rates as illustrated in Fig. 6. This does not only “save computation time” but allows to track a moving input at a high rate since convergence to the modified state is improved. As far as biological neural maps are understood the convergence of the neural field towards a new state is not the result of the convergence of a progressive iterative process, but a tip over from one state to another when the input changes.

Here, our study shows how to adjust δ in order to obtain optimal convergence rate, thus optimally track a moving input.

What we have numerically experimented with the conditions reported in Fig. 2 (thus with $|\bar{\mathbf{W}}^+| = 0.0$), is that the tracking of a moving bump is optimally tracked for $\delta \simeq 1/2$.

Application to remanence.

Short-term memory behavior is related to the capability to maintain the output for a short period of time, even if the input vanishes. This is a behavior inverse from the previous one, since we do not require the system to quickly converge to the new state (corresponding to a null input), but remains in the old state (related to the previous input).

In our framework this may correspond to $|\bar{\mathbf{W}}^+| \geq 1$, as shown, in the linear case, by the formula (4) and experimented numerically in Fig. 5, for $1 \leq |\bar{\mathbf{W}}^+| \leq \simeq 1.5$. If $|\bar{\mathbf{W}}^+| \geq 1$, the linear transfer function has ‘‘poles’’ (corresponding to resonances in oscillatory regimes), i.e. unbounded output for infinitesimal inputs. Numerically, this corresponds to high-gains (corresponding to damped resonances in oscillatory regimes), and slow time decays, as required for such behavior. Tuning the scheme parameters in this range allows to approximate remanence, although this yields solutions at the edge of instability.

Another strategy is to consider not a rectification but a piece-wise linear sigmoid profile as shown in Fig. 1 and consider $|\bar{\mathbf{W}}^+| \geq 1$. In that case the scheme tends to increase the output or yield divergence, but because of the saturation, the output remains bounded. This allows to easily generate remanence, as it is observed in numerical simulations [21], and the behavior is more robust. The add-on of the previous derivations allows to know the scheme parameters range to obtain this behavior.

4 Results about the bumps

Analysis of the fixed point equation.

Let us now discuss how to obtain, at the implementation level, bumps with controlled shapes. Since there is a fixed point converging dynamics, we simply have to consider the fixed point equation in this section. The scheme (2) or (3) fixed point equation writes, given a radial input $\mathbf{i}(|\mathbf{x}|)$ and output $\mathbf{u}(|\mathbf{x}|, +\infty)$:

$$\bar{\mathbf{z}} = \bar{\mathbf{U}}^+ \bar{\mathbf{W}} + (\bar{\mathbf{i}} - \bar{\mathbf{u}}^+ - \bar{\mathbf{u}}^- / \delta) = 0 \quad (6)$$

with $\bar{\mathbf{u}}^+ = \rho(\bar{\mathbf{u}}) = \max(0, \bar{\mathbf{u}})$ and $\bar{\mathbf{u}}^- = \rho(-\bar{\mathbf{u}}) = \min(0, \bar{\mathbf{u}})$, thus $\bar{\mathbf{u}} = \bar{\mathbf{u}}^+ + \bar{\mathbf{u}}^-$, while:

$$\mathbf{U}_k^+(|\mathbf{x}|) = \sum_{\mathbf{y}, |\mathbf{y}|=r_k} \mathbf{u}^+(|\mathbf{x} - \mathbf{y}|)$$

defines the convolution in the discrete case. In the 2D case for instance, for weights defined in a bounded circular neighborhood of radius R , this convolution writes:

$$\begin{aligned} [\bar{\mathbf{U}}^+ \bar{\mathbf{W}}](x, y) &= \sum_{k=1}^K W[k] \sum_{(i,j), i^2+j^2=r_k^2 \leq R^2} u(x-i, y-j) \\ &= W[1]u(x, y) + W[2](u(x+1, y) + u(x-1, y) + u(x, y+1) + u(x, y-1)) + \dots \end{aligned}$$

as represented in Fig. 7 for $R = 5$, while it is obvious, from a piece of symbolic computation, to derive for any R the K related terms, with:

R	1	2	3	4	5	6	7	8	9	10	11	12	13	14	15	16	...
K	2	4	7	10	14	19	24	30	37	44	52	59	69	78	87	98	...

showing a supra-linear and sub-quadratic (numerically $K = O(R^{\simeq 1.7})$) increase of the number of radial coefficients.

This fixed-point equation splits in two parts:

$$\begin{aligned} \mathbf{u}(|\mathbf{x}|) > 0 \quad \bar{\mathbf{z}}_{|\mathbf{x}|} &= [\bar{\mathbf{U}}^+ \bar{\mathbf{W}} + (\bar{\mathbf{i}} - \bar{\mathbf{u}}^+)]_{|\mathbf{x}|} \Rightarrow [1 - \bar{\mathbf{W}}] \mathbf{u}^+(|\mathbf{x}|) = \mathbf{i}(|\mathbf{x}|) \\ \mathbf{u}(|\mathbf{x}|) \leq 0 \quad \bar{\mathbf{z}}_{|\mathbf{x}|} &= [\bar{\mathbf{U}}^+ \bar{\mathbf{W}} + (\bar{\mathbf{i}} - \bar{\mathbf{u}}^- / \delta)]_{|\mathbf{x}|} \Rightarrow [1 - 1/\delta - \bar{\mathbf{W}}] \mathbf{u}^+(|\mathbf{x}|) \leq \mathbf{i}(|\mathbf{x}|) \end{aligned}$$

i.e.:

0	0	0	0	0	14	0	0	0	0	0	0	0	0
0	0	14	13	11	10	11	13	14	0	0	0	0	0
0	14	12	9	8	7	8	9	12	14	0	0	0	0
0	13	9	6	5	4	5	6	9	13	0	0	0	0
0	11	8	5	3	2	3	5	8	11	0	0	0	0
14	10	7	4	2	1	2	4	7	10	14	0	0	0
0	11	8	5	3	2	3	5	8	11	0	0	0	0
0	13	9	6	5	4	5	6	9	13	0	0	0	0
0	14	12	9	8	7	8	9	12	14	0	0	0	0
0	0	14	13	11	10	11	13	14	0	0	0	0	0
0	0	0	0	0	14	0	0	0	0	0	0	0	0

k	1	2	3	4	5	6	7	8	9	10	11	12	13	14
r_k	0	1	$\sqrt{2}$	2	$\sqrt{5}$	$\sqrt{8}$	3	$\sqrt{10}$	$\sqrt{13}$	4	$\sqrt{17}$	$\sqrt{18}$	$\sqrt{20}$	5

Figure 7: Representation of the radial symmetric discrete convolution indexing in the 2D case for a bounded circular neighborhood of radius $R = 5$. The 2D locations of the indexes are drawn in the top array and the correspondence between index and radius in the bottom table. This indexing has been derived using a piece of symbolic computation `maple` code, also allowing to automatically generates the optimal numerical C/C++ code for any convolution of radius R .

- A *linear response* for points inside the bump (with $\mathbf{u}(|\mathbf{x}|) > 0$), which does not depend on δ , and is related to the output response adjustment.
 - An *adaptive threshold* cut-off mechanism outside the bump (with $\mathbf{u}(|\mathbf{x}|) \leq 0$), which allows to perform selection, and is related to input inhibition control.
- The key point is that, *given a desired output \mathbf{u}^+ , the equation is linear with respect to the weights \mathbf{W}* .
 - Furthermore, δ simply scales the inhibited part of the output \mathbf{u}^- and is thus not an independent parameter.
 - Here \mathbf{u}^-/δ is a hidden parameter of the problem: It allows to specify the level of inhibition against input perturbations.
 - There is a scale invariance, in the sense that multiplying input and output by the same scale factor, does not change the equation with respect to \mathbf{W} . We thus are going to consider, without any loss of generality, normalized input in the sequel, i.e. considering the *volume*:

$$V(\mathbf{i}) = \sum_{\mathbf{x}} |\mathbf{i}(\mathbf{x})| \quad (7)$$

input with $V(\mathbf{i}) = 1$.

- Finally, the output response adjustment is entirely defined by the input-output difference $[\bar{\mathbf{i}} - \bar{\mathbf{u}}^+]_{|\mathbf{x}|, \mathbf{u}(|\mathbf{x}|) > 0}$, which is yet another simplification of the problem structure.
- Given these properties, let us now formalize the output control.

Position of the problem.

The fact we want to “tune” the weights \mathbf{W} , as illustrated in Fig. 8, can be formulated as follows: *Given a set of input $\bar{\mathbf{i}}_l$, indexed by l and a set of corresponding desired output $\bar{\mathbf{u}}_l^+$, the goal is to find the desired optimal weights \mathbf{W} that maps the input onto the output.*

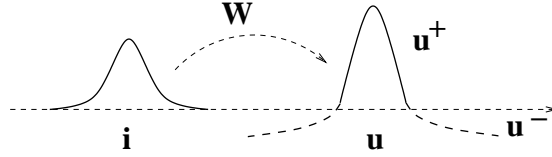


Figure 8: Schematic representation of the problem position: given one input \mathbf{i} (or a set of) and the related desired output \mathbf{u}^+ , the goal is to find the optimal weights \mathbf{W} . The inhibited output \mathbf{u}^- is a hidden parameter of the problem.

This can be turned into a variational specification: *Given an input-output set* $\{\dots(\bar{\mathbf{i}}_l, \bar{\mathbf{u}}_l^+) \dots\}$, *the optimal weights minimize:*

$$\mathcal{C} = \sum_l \sum_{|\mathbf{x}|} |\mathbf{z}_{|\mathbf{x}|,l}|_{\Lambda_{|\mathbf{x}|,l}}^2 + \sum_{\mathbf{y}} |\nabla \mathbf{W}(\mathbf{y})|_{\mathbf{L}}^2 \quad (8)$$

where:

- The output error $\mathbf{z}_{|\mathbf{x}|,l}$ magnitude at point $|\mathbf{x}|$ for the input-output sample of index l (defined in (6)) is minimized, up to some pondering matrix $\Lambda_{|\mathbf{x}|,l}$ allowing to take into account the relative importance of a sample of index l and a map location \mathbf{x} .
- The weights are regularized in the sense that the weight's gradient $\nabla \mathbf{W}$ is also minimized, up to some pondering matrix \mathbf{L} , allowing to avoid ill-posed specifications.

Here, for the sake of simplicity, we consider quadratic norms, yielding linear equations for the extrema, although in this finite discrete case, other norms are rather easy to introduce.

This specification allows to immediately derive:

$$\left[\sum_l (\bar{\mathbf{U}}_l^+)^T \bar{\Lambda}_l \bar{\mathbf{U}}_l^+ \right] \bar{\mathbf{W}} = \sum_l (\bar{\mathbf{U}}_l^+)^T \bar{\Lambda}_l [\bar{\mathbf{i}}_l - \bar{\mathbf{u}}_l^+ - \bar{\mathbf{u}}_l^- / \delta] + \Delta_{\mathbf{L}} \mathbf{W} \quad (9)$$

writing $\bar{\Lambda}_l$ the block-diagonal matrix defined by $\Lambda_{|\mathbf{x}|,l}$, while $\Delta_{\mathbf{L}} \mathbf{W}$ is the discrete Laplace operator accounting for the regularization term. Here we deliberately use oversimplified notations for this very standard regularization mechanism $\Delta_{\mathbf{L}} \mathbf{W}$, see e.g., [24] for further technical details.

Specification of the estimation parameters.

The hidden variable $\bar{\mathbf{u}}_l^- / \delta$ is defined at points where $\mathbf{u}(|\mathbf{x}|) \leq 0$ and can be derived from (8):

$$[\sum_l \bar{\Lambda}_l^-] \bar{\mathbf{u}}_l^- / \delta = \sum_l \bar{\Lambda}_l^- [\bar{\mathbf{U}}_l^+ \bar{\mathbf{W}} + \bar{\mathbf{i}}_l],$$

writing $\bar{\Lambda}_l^-$ the block-diagonal matrix defined by $\Lambda_{|\mathbf{x}|,l}^- = (\text{if } \mathbf{u}(|\mathbf{x}|) \leq 0 \text{ then } \Lambda_{|\mathbf{x}|,l} \text{ else } 0)$, i.e., taking only points with $\mathbf{u}(|\mathbf{x}|) < 0$, thus where $\bar{\mathbf{u}}^-$ is defined, into account. This yields after a few algebra:

$$\left[\sum_l (\bar{\mathbf{U}}_l^+)^T \left[\bar{\Lambda}_l - \bar{\Lambda}_l [\sum_l \bar{\Lambda}_l^-]^\dagger \bar{\Lambda}_l \right] \bar{\mathbf{U}}_l^+ \right] \bar{\mathbf{W}} = \sum_l (\bar{\mathbf{U}}_l^+)^T \bar{\Lambda}_l^+ [\bar{\mathbf{i}}_l - \bar{\mathbf{u}}_l^+] + \Delta_{\mathbf{L}} \mathbf{W},$$

writing $\bar{\Lambda}_l^+$ the block-diagonal matrix defined by $\Lambda_{|\mathbf{x}|,l}^+ = (\text{if } \mathbf{u}(|\mathbf{x}|) > 0 \text{ then } \Lambda_{|\mathbf{x}|,l} \text{ else } 0)$, while \mathbf{M}^\dagger is the pseudo-inverse of the matrix \mathbf{M} . This last equation, entirely defined from (8), specifies the weights \mathbf{W} as a function of \mathbf{i} and \mathbf{u}^+ .

Let us discuss this last point. The pondering matrix $\Lambda_{|\mathbf{x}|,l} \geq 0$ defines, for each point and sample, the relative weight of the estimation (in other words the ‘‘estimation

gain” for this point and sample). A zero value allows to eliminate the related measure in the estimation process, a high value to make it important. For scalar maps ($m = 1$) $\Lambda_{|\mathbf{x}|,l} \geq 0$ is a number, otherwise it is a $m \times m$ positive symmetric matrix. As far as $\bar{\Lambda}_l^+$ is concerned (i.e., for point with $\mathbf{u}(|\mathbf{x}|) > 0$), this corresponds to pondering the output value, which is an interesting feature. As far as $\bar{\Lambda}_l^-$ is concerned (i.e., for point with $\mathbf{u}(|\mathbf{x}|) < 0$), this corresponds to pondering the “absence” of the output value, i.e. the inhibition level. This inhibition level is thus not tuned here though a value but though a kind of “estimation gain”. An alternative, at the specification level, would be to *simply specify* \mathbf{u}^-/δ , i.e. the inhibition value itself: This is very easy to introduce in (9) which is now the linear equation defining \mathbf{W} .

This specification choice has also a computational advantage, since using (9) is numerically more stable than the previous equation: If \mathbf{u}^-/δ is not specified as an income of the problem, the previous derivation corresponds to eliminating \mathbf{u}^-/δ (solving (8) where $\mathbf{u}(|\mathbf{x}|) < 0$, thus considering input inhibition) and reintroduced the result in order to find \mathbf{w} (solving (8) where $\mathbf{u}(|\mathbf{x}|) > 0$, thus considering output adjustment). If \mathbf{u}^-/δ is directly specified, then (9) allows us to linearly combine both output control and adjustment inhibition in the estimation.

A step further, equation (9) is a “Hebbian” equation in the following sense: it is local and only depends on the output value and linearly on the input value. In the present study, for the sake of simplicity, we implicitly assume that the weights \mathbf{W} do not depend on $|\mathbf{x}|$. However, this is not a limitation of the method: The criterion (8) is still well-defined in the more general case of non-constant weights. Then, equation (9) is “local” in the sense that $\bar{\mathbf{U}}_l^+$ only depends on the output values “around” \mathbf{x} (more precisely in a neighborhood corresponding to the size of the output bump) while it only linearly depends on the input at point \mathbf{x} . This is not the case if we do not introduce \mathbf{u}^-/δ as an income of the problem.

As a consequence, we propose to use (9) in the sequel. Furthermore, for the sake of simplicity, we are going to consider $\bar{\Lambda} = \mathbf{I}$ (no pondering), while we simply consider a singleton of input-output couple. The idea is to validate and study the method in a relatively simple case, before making profit of it at its whole level of generality.

Parametric 2D scalar piece-wise constant weights adjustment.

In order to apply the previous framework we start considering the simplest possible radial symmetric weights profile:

$$W(|\mathbf{y}|) = \text{if } |\mathbf{y}| < S \text{ then } +W_0 \text{ else } -W_1$$

in words an excitatory flat constant profile of magnitude W_0 in a central area of radius S and a spatially unbounded flat constant inhibitory profile of magnitude W_1 outside the disk of radius S , as illustrated in Fig. 9.

This is thus a parametric weight profile, parametrized with $\phi = (W_0, S, W_1)$.

We further assume that $S \ll R$, R being the bump radius, i.e., that the excitatory weights radius is small with respect to the bump size, which allows to derive an approximate closed-form for the input-output relation.

More precisely, this allows to write after a few algebra:

$$\begin{aligned} \mathbf{u}(r = |\mathbf{x}|) &= \sum_{|\mathbf{x}-\mathbf{y}| < S} \mathbf{u}(|\mathbf{y}|) \\ &= \mathbf{W}_{[0, R-S]}(r) \left[\pi S^2 \mathbf{u}(r) - \frac{\pi S^4}{2} + O(S^6 + S^4 r^2) \right] + \mathbf{W}_{[R-S, R+S]}(r) v(r^2) \end{aligned} \quad ,$$

with $\mathbf{W}_{[a,b]}(r) = \text{if } a \leq r \leq b \text{ then } 1 \text{ else } 0$ while $v(r^2)$ is a term neglected in the sequel, since $S \ll R$.

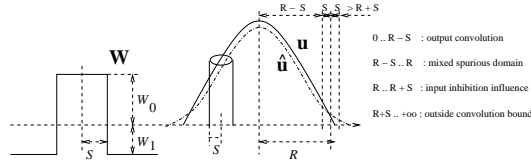


Figure 9: *Left view*: Radial symmetric piece-wise constant weight parameters profile, W_0 being the central excitatory magnitude, W_1 the peripheral inhibitory magnitude, while S is the radius of the circle separating both weight's regions. *Right view*: Schematic representation of the convolution of a bump u of radius R by a radial symmetric sum of radius $S \ll R$. The result \hat{u} is decomposed in four zones, as made explicit in the right part of the diagram, and obtained when deriving the closed form approximation of this convolution.

This leads to the following closed-form formulas:

$$\begin{cases} \mathbf{u}(r) = \alpha^{-1} (\mathbf{i}(r) - \beta \mathbf{i}) + O(S^4) & r \in [0, R - S] & \text{linear response} \\ \mathbf{i}(r) \leq \beta \mathbf{i} + O(S^4) & r \in [R + S, +\infty] & \text{threshold inhibition} \end{cases}$$

with $\alpha \stackrel{\text{def}}{=} 1 - \pi (W_0 + W_1) S^2$ and $\beta \stackrel{\text{def}}{=} (\alpha + \pi W_1 R^2)^{-1} W_1$ while $\mathbf{i} = \sum_{|y| < R} \mathbf{i}(|y|)$.

Let us derive the linear response equation. If $\mathbf{u}(r = |\mathbf{x}|) > 0$:

$$\begin{aligned} \mathbf{u}(\mathbf{x}) &= \sum_{\mathbf{y}} \mathbf{W}(\mathbf{x} - \mathbf{y}) \mathbf{u}(\mathbf{y}) + \mathbf{i}(\mathbf{x}) \\ &= \mathbf{W}_0 \sum_{\mathbf{y}, |\mathbf{x} - \mathbf{y}| < S} \mathbf{u}(\mathbf{y}) - \mathbf{W}_1 \sum_{\mathbf{y}, |\mathbf{x} - \mathbf{y}| \geq S} \mathbf{u}(\mathbf{y}) + \mathbf{i}(\mathbf{x}) \\ &= (\mathbf{W}_0 + \mathbf{W}_1) \sum_{\mathbf{y}, |\mathbf{x} - \mathbf{y}| < S} \mathbf{u}(\mathbf{y}) - \mathbf{W}_1 \sum_{\mathbf{y}} \mathbf{u}(\mathbf{y}) + \mathbf{i}(\mathbf{x}) \\ &= (\mathbf{W}_0 + \mathbf{W}_1) \hat{\mathbf{u}}(\mathbf{x}) - \mathbf{W}_1 \hat{\mathbf{u}} + \mathbf{i}(\mathbf{x}) \end{aligned}$$

writing $\hat{\mathbf{u}} = \sum_{\mathbf{y}} \mathbf{u}^+(\mathbf{y}) = \sum_{\mathbf{y}, |\mathbf{y}| < R} \mathbf{u}(\mathbf{y})$.

Considering the approximation $\hat{\mathbf{u}}(r = |\mathbf{x}|) \simeq W_{[0, R-S]}(r) \pi S^2 \mathbf{u}(r) + O(S^4)$ allows to further write:

$$\mathbf{u}(\mathbf{x}) = \pi (\mathbf{W}_0 + \mathbf{W}_1) S^2 \mathbf{u}(\mathbf{x}) - \mathbf{W}_1 \hat{\mathbf{u}} + \mathbf{i}(\mathbf{x}) + O(S^4)$$

thus:

$$\hat{\mathbf{u}} = \sum_{\mathbf{x}, |\mathbf{x}| < R} \mathbf{u}(\mathbf{x}) = \pi (\mathbf{W}_0 + \mathbf{W}_1) S^2 \hat{\mathbf{u}} - \mathbf{W}_1 \pi R^2 \hat{\mathbf{u}} + \mathbf{i} + O(S^4)$$

considering $\sum_{\mathbf{x}, |\mathbf{x}| < R} 1 \simeq \int_{\mathbf{x}, |\mathbf{x}| < R} 1 = \pi R^2$, leads to the linear response equality, written above in the scalar case.

Otherwise, if $\mathbf{u}(r = |\mathbf{x}|) \leq 0$ and $|\mathbf{x}| > R + S$:

$$\begin{aligned} \sum_{\mathbf{y}} \mathbf{W}(\mathbf{x} - \mathbf{y}) \mathbf{u}(\mathbf{y}) + \mathbf{i}(\mathbf{x}) &\leq 0 \\ \mathbf{W}_1 \hat{\mathbf{u}} + \mathbf{i}(\mathbf{x}) &\leq 0 \end{aligned}$$

leads to the threshold inhibition inequality.

In order this equation to be well defined, we must have:

$$\pi (W_0 + W_1) S^2 < 1,$$

which is in direct relation with the convergence condition (but does not correspond to it, since we use an approximation here).

This derivation is informative and shows that, up to the proposed approximation, the response is mainly a thresholding mechanism: the effect of the computation is to cut the input under the given threshold, thus eliminating spurious distractors of the main input bump and reducing also the output volume. The calculation is non trivial because the threshold $\beta \mathbf{i}$ is adaptive and related to the input volume around the output bump. The radius R of the output bump is an implicit parameter depending on the weight parameters, thus not easy to read on the formula. These aspects are further detailed and verified numerically in Fig. 10 and Fig. 11, providing also some abacus to choose the desired output bump.

Non-parametric 2D scalar spatial-bounded weights adjustment.

In this second numerical application, we consider non-parametric 2D scalar spatial-bounded symmetric radial weights, as made explicit in Fig. 7.

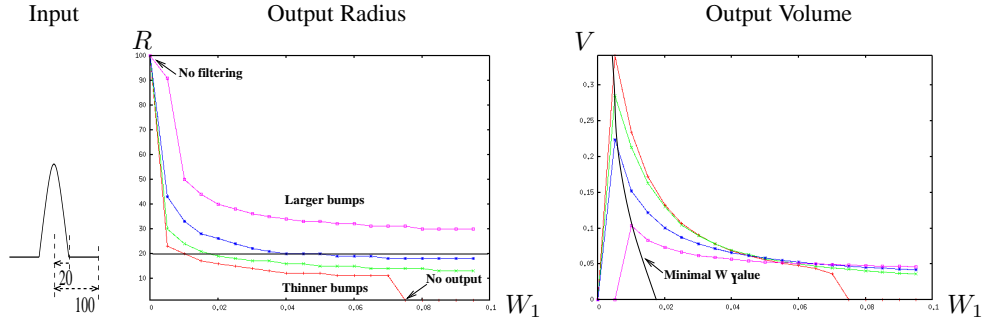


Figure 10: Numerical verification of the capability to control the output radius and volume, for a normalized input profile of radius 20 and a 2D 100×100 scalar map. The weight radius values are $S = \{2$ (red), 5 (green), 10 (blue), 20 (magenta) $\}$ while the excitatory magnitude W_0 is adjusted from S in order to have $|\mathbf{W}| = 0.99$. The inhibitory magnitude varies in $W_1 \in [0, 0.1]$. When $W_1 = 0$ there is no filtering (output equals input). If W_1 is too small the excitatory weights diffuse the input all over the map. If W_1 is too high (as for $S = 2$ and $W_1 > 0.073$) inhibition is high enough to cancel the whole input. Larger S increase diffusion of the input thus enlarge the output radius. Higher inhibition magnitudes W_1 increase the thresholding thus decrease the output radius. The output volume is also obviously controlled by the input gain (taken as 1 in the derivation to ease the notations).

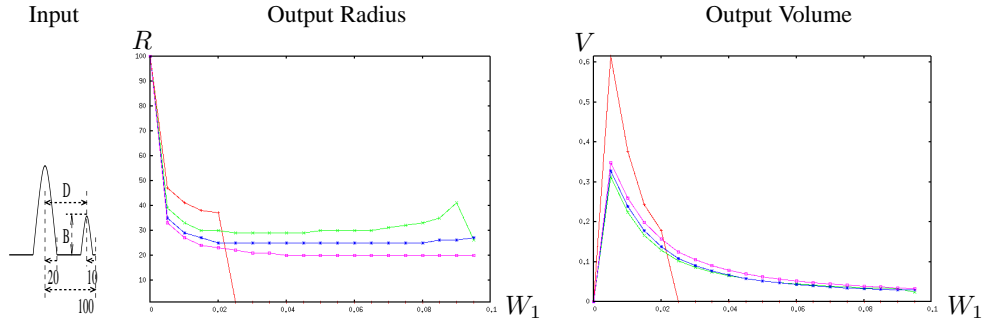


Figure 11: Numerical verification of the capability to perform selection between the main input and distractors, for a normalized input profile of radius 20 and a 2D 100×100 scalar map, plus a distractor of width 10, height B and eccentricity D . Here the radius is fixed $S = 5$ and the excitatory magnitude W_0 to have $|\mathbf{W}| = 0.99$. The inhibitory magnitude varies in $W_1 \in [0, 0.1]$. The green curves correspond to $D = 20, B = 0.9$, the blue curve to $D = 15, B = 0.9$, and the magenta curve to $D = 10, B = 0.9$. The selection mechanisms (comparing the results with those of Fig. 10) clearly works and we obtain similar results, as predicted by the previous derivation, since the input dependence is mainly related to the input volume in the output radius disk. Small variations qualitatively correspond to this radius variability. The red curves correspond to $D = 20, B = 10$ thus the distractor is higher than the central bump and the selection fails, as expected. In this latter case, when inhibition increases, the overall amount of input yields an output extinction.

Now the profile is parametrized by the radial values $W[i], i \in \{1, K\}$. In order to instantiate the general method proposed in (8) and (9), we fix a form for the input and output, presently:

$$\begin{aligned} \mathbf{u}(r) &= A H(R - r) 2/\pi [R^2 - r^2]/R^4 + H(r - R) T \left[e^{-(4/\pi A/(R^3 T))(r-R)} - 1 \right] \\ \mathbf{i}(r) &= H(C - r) 2/\pi [C^2 - r^2]/C^4 \end{aligned}$$

thus quadratic input and output profiles with predefined parameters, as detailed in Fig. 12, while the inhibited profile is exponential and chosen in order \mathbf{u} to remains \mathcal{C}^1 .

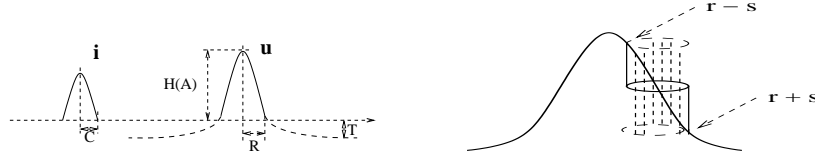


Figure 12: Schematic representation of the two main elements of the numerical set-up. *Left view*: An “generic” input of radius C and volume 1 in correspondence with a generic output of height H corresponding to a volume A and radius R is chosen. The level of inhibition is fixed by an additional parameter T corresponding to the asymptotic value of the inhibited activity. *Right view*: A schematic representation of the numerical integration of the convolution at a given radial location.

The numerical approximation of the convolution writes:

$$\mathbf{U}_s(r) \simeq 2\pi s \sum_{\theta} u^+(r^2 - 2rs \cos(\theta) + s^2) / \sum_{\theta} 1$$

as illustrated in Fig. 12.

The general criterion (8) simply writes in this case:

$$\min_{\mathbf{W}} |\bar{\mathbf{z}}| + L \sum_s d\mathbf{W}[s]^2$$

for a regularization parameter L .

Numerical results are reported and discussed in Fig. 13.

Application to inhibition control of the output radius.

As a final numerical application, let us consider parametric 2D scalar Mexican-hat symmetric radial weights, as made explicit in the section 2.

We reuse the previous form of input and output (bounded quadratic response and exponential inhibition) with $A = 1$ since the output volume control is easily tuned by the input gain. We fix $T = 1$ since it has been observed that this parameter value is not critical. We further do not consider regularization ($L = 0$) since the profile is parametric thus de-facto regular.

Since we are interested here in controlling the output radius, we are going to explore the relation between the input radius C and the output radius R .

Regarding the Mexican hat profile, we consider that the weight width parameters σ_+ and σ_- are structural parameters, thus fixed by the connectivity. A step further, since we are interested in selection and remanence we choose $|\mathbf{W}^+| = 0.9$ so that the excitatory weights magnitude $|A^+|$ is fixed from σ_+ as detailed previously.

We are thus left with controlling the inhibitory weights magnitude $|A^-|$ obtaining results given in Fig. 14. The interesting conclusion is that Mexican-hat profiles (compared to the previous profiles) are far from being optimal to control the output radius. Sharp profiles (i.e. with excitatory/inhibitory weights clearly separated) seem a better choice. Furthermore, not the magnitude but the width of the inhibition is the best control variable to adjust the output radius.

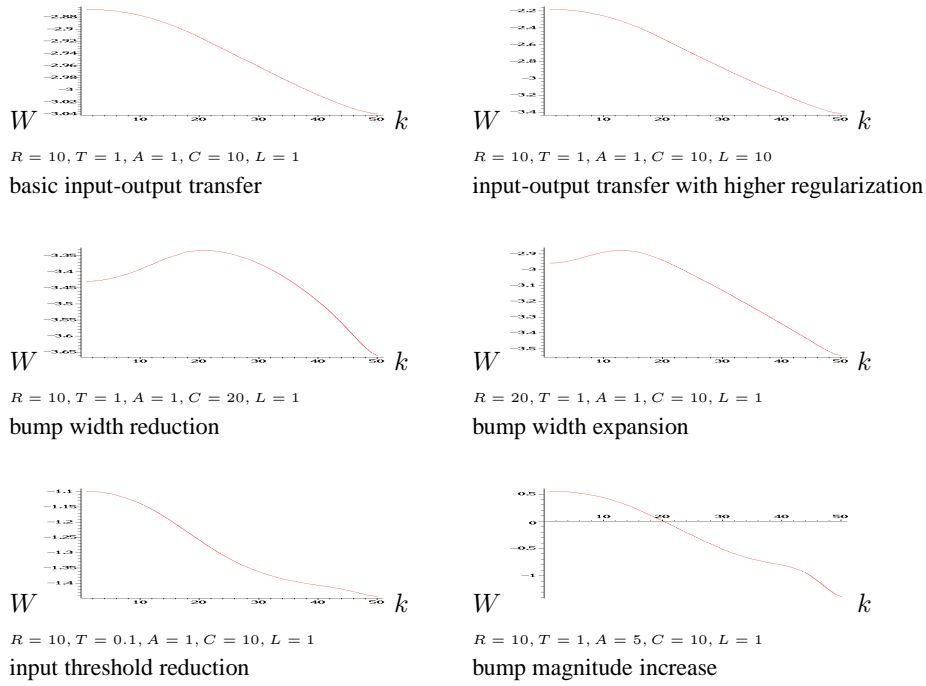


Figure 13: Numerical results for non-parametric weights adjustment, here for $W[k], k \in \{1, 50\}$. The *top-left* curve corresponds to a standard input-output transfer, and the optimal weights correspond to pure inhibitory profiles, which corresponds to the usual practice of experimenters. However, the obtained shape might be counter-intuitive in the sense that inhibition only increases with eccentricity up to the weights spatial bounds, without any decrease for high eccentricities. The *top-right* curve corresponds to a standard input-output transfer, but estimated with a much higher regularization parameter L . The nice result is that the shape is a bit smoother as expected, but in fact only marginally depends on this extra parameter, which is non critical as soon as set to a reasonable value. The *middle-left* curve corresponds to an output radius reduction with respect to the input radius, while the *middle-right* curve corresponds to an output radius expansion, which appears to be obtained by a non monotonic shape, according to the proposed criterion. The *bottom-left* curve corresponds to the choice of a lower inhibition level T , again showing the non-critical impact of this parameter, except an expected reduction of the inhibition weights magnitude. The *bottom-right* curve correspond to bump magnitude amplification, which is coherent with the apparition of excitatory weights in this case. All profiles must verify $|\mathbf{W}| < 1$ since they map bounded input onto bounded output, thus in a case where the scheme is converging.

5 Discussion and conclusion

The previous results do not “prove” the existence of stable bump solutions, this being already known [27, 2] and extensively verified numerically. Here the goal is to calculate algorithmically the related parameters. This modest objective is attained since we now are able to tell which parameter set yields convergence and how to control the output and the shape of the bump.

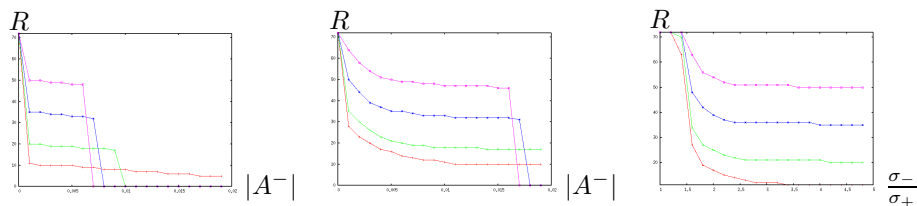


Figure 14: Numerical verification of the capability to control the output radius with inhibition adjustment. The input radius values are $C = \{10 \text{ (red)}, 20 \text{ (green)}, 35 \text{ (blue)}, 50 \text{ (magenta)}\}$. The inhibitory magnitude varies in $|A^-| \in [0, 0.02]$ while other parameters are adjusted as discussed in the text. *Left view:* $\sigma_-/\sigma_+ = 5$. The result is somehow negative: the output radius is always smaller than the input radius and has only tight variations (in the range where the inhibition is high enough to perform filtering and small enough to avoid the output extinction). *Middle view:* $\sigma_-/\sigma_+ = 1.5$. The result is now less negative: the output radius can be controlled by inhibition adjustment. However the output radius is always higher than the input radius. *Right view:* Here $|A^-| = 0.01$ and the $\sigma_-/\sigma_+ \in [1, 5]$ is varied. It appears clearly that this controlled variable is much more efficient to adjust the output radius.

Further applications of bump control.

One track is to consider how tuning distributed propagation delays and also feedback delays [3] can, at the implementation level, control bumps but also traveling fronts [16]

Application to other paradigms.

In a recent work [20] a model has been designed that performs global competition, only using local connections, with diffusion of the inhibition throughout the network. This is far quicker to have a few local interactions when computing activity within the network and makes the model a real candidate for distributed computations. This paradigm is taken into account here, with non-parameteric weight adjustments.

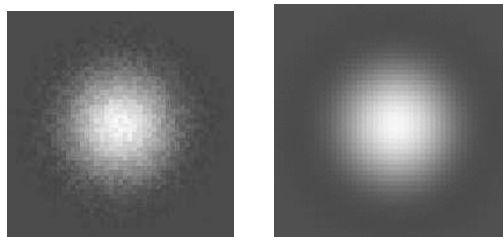


Figure 15: An example of asynchronous sampling of such maps (event-based implementation), applying convergence criteria derived here. We have numerically verified the conjecture that the present results apply when using asynchronous sampling. *Left view:* intermediate result, the fact asynchronous sampling yields randomization is visible. *Right view:* final result, after convergence.

A slight modification of the previous derivation, allows to not only consider synchronous but asynchronous sampling (see [21] for details) since the map is still contracting when using asynchronous sampling. This has been numerically experimented,

as shown in Fig. 15 and has to be further investigated. Interesting enough is the fact that this simulation has been implemented on an event-based neural network simulator, in order to consider neural maps not as simple “analog” calculations, but both analog and event-based [19].

We have proposed the numerical results only for 2D scalar maps, for the simple reason we are publishing these results . . . on a 2D scalar support. All derivations have been developed for the vectorial case and are thus available for higher-dimensional paradigms.

Here we have restrained the discrete scheme to (2) with $0 < \delta < 1$. It is an interesting perspective to consider convergence and output control for $1 \leq \delta < 2$ or higher values.

Beyond parameter adjustment.

Beyond such technical variants, the idea is to get rid of continuous schemes of the form (1), whereas directly study to which extends a discrete dynamical system of the form (2) is of interest to analyze and simulate the neural maps behaviors. This is, for instance, the case in [22] where the dynamics of spiking and spiking-bursting activity of real biological has been studied via a discrete two-dimensional map defined with one fast and one slow variable. As a consequence, discretized neural fields power of description is still to be explored for both distributed computational paradigms and biologically plausible computational map models

A Tuning bumps in the linear case

Bump as required output In this context, the desired output profile is a bump, i.e. a *positive, decreasing, radial symmetric profile*, as observed for bubble of activities in the cortex [2, 11]. A Gaussian profile is one example of bump. In order to capture the notion of bump at a more general level, we propose to consider Gaussian enumerable linear combinations, i.e. *Gaussian series*:

$$\mathbf{b}(\mathbf{p}) = \sum_{s \in \{s_1, \dots\}, s > 0} \mathbf{b}^*(s) e^{-s |\mathbf{p}|^2},$$

writing $s = \frac{1}{2\sigma^2}$ for an enumerable set of “width” s , which is of common use (e.g. [26]). Small s for flat Gaussian ($s = 0$ is the “constant part”), Large s for tight Gaussian.

The goal is thus to find the parameters allowing to generate bumps, controlling their width, amplitude and shape.

Let us now discuss how to obtain, at the implementation level, bumps with controlled shapes, in the linear case.

Gaussian series approximate bumps. Radial symmetric profile means that $\mathbf{b}(\mathbf{p}) = \beta(|\mathbf{p}|^2)$, normalized iff $\int_{\mathbf{p}} b_i(\mathbf{p}) = 1$. They are positive iff $\beta_i(r) \geq 0$ and decreasing iff $\beta_i'(r) \leq 0$. This puts our specifications in equation.

For Gaussian series:

$$\beta(r) = \sum_s \mathbf{b}^*(s) e^{-s r} = \mathcal{L}(\mathbf{b}^*)(r)$$

where \mathcal{L} stands for the Laplace transform, while \mathbf{b}^* has been extended to the continuum

using a Dirac comb, while the Post-Bryan inversion formula⁸ [5] allows to consider the Laplace transform of such positive functions.

This observation means that *bumps can be approximated using Gaussian series* for the simple reason that Gaussian series coefficients are nothing but the discrete approximation of the bump β profile's Laplace transform. This representation thus benefits from all the Laplace transform properties:

Bump are normalized iff $\int_{s>0} b_i^*(s)(\pi/s)^{n/2} = 1$. Several additional properties characterize such bumps: they are flat at 0 unless singular (i.e. $|\mathbf{b}(\mathbf{0})| < +\infty \Rightarrow |\nabla \mathbf{b}(\mathbf{0})| = 0$), vanish at infinity ($\lim_{r \rightarrow +\infty} \beta(r) = 0$) thus without constant component ($\lim_{s \rightarrow 0} b^*(s) = 0$), etc..

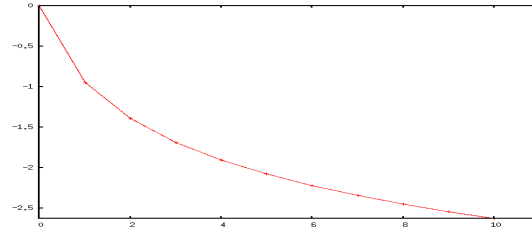


Figure 16: An example of maximal gain curve in the non-linear case. Given σ_+ in abscissa (in pixel unit for a 100×100 2D map), the normalized maximal value of $\log_{10}(|\mathbf{A}_+|)$ is drawn. Here, not a Mexican hat but a step-wise constant profile has been used, since the derivation can be performed with any W profile.

Gaussian series yield “nice” bumps. The previous result is useful because it is very easy to shape the bump using suitable coefficients, for instance using rational profiles of the form $\beta_1(r) = 1/(1 + |r|^{n/2})$, n even since:

$$\begin{aligned} b_1(s)^* &= \frac{1}{n} \sum_{i=1}^n e^{-s \sin(\alpha_n^i)} \sin(s \sin(\beta_n^i) + \alpha_n^i) \\ \alpha_n^i &= \frac{\pi}{n} \left(2i + \frac{n}{2} - 1\right) \\ \beta_n^i &= \frac{\pi}{n} (1 - 2i) \end{aligned}$$

or of the form $\beta_2(r) = 1/r^n$, $n > 0$ since:

$$b_2(s)^* = s^{n-1}/n - 1!$$

as illustrated in Fig. 17. Such profiles correspond to desired bumps in neural field applications, among many other suitable alternatives. They come with closed-form formula and show how malleable are such shapes.

Note that a simple change of scale allows to adjust the width and the amplitude of the bump, the challenge here being to adjust the *shape*.

Gaussian series are linear map fix points. Linear map fixed points \mathbf{u}^\bullet are defined by $-\mathbf{u}^\bullet + \mathbf{W} * \mathbf{u}^\bullet + \mathbf{i} = 0$, where $*$ stands for the convolution operator. Since convolution and linear combination of Gaussian are Gaussian, *providing that the input \mathbf{i} and the weights profile \mathbf{W} are Gaussian series, the output \mathbf{u}^\bullet is a Gaussian series*. This result is made explicit by the following formula for the Gaussian series coefficients:

$$-\mathbf{u}^\bullet(\nu) + \pi \sum_{r>\nu, s>\nu, \frac{r+s}{r+s}=\nu} \frac{W(r)u^\bullet(s)}{r+s} + i(\nu) = 0,$$

⁸Post-Bryan result: A continuous function on \mathcal{R}^+ which is of exponential order for some c (i.e. $\|b(r)\|/e^{cr} \Big|_{\infty} < \infty$) with Laplace transform $b^*(s)$ is non-negative iff $\forall k \geq 0, \forall s \geq c, (-1)^k b^{*(k)}(s) \geq 0$.

This is true for rather general weight profiles, not necessarily “Mexican-hat” profile only.

In this specific case, it is possible to derive a closed-form expansion, convergent as soon as $|A_{\pm}| < 1$, which is the case in practice. We obtain up to a given order r :

$$u^{\bullet}(\nu) = \frac{\sum_s i(s) \sum_{p,q,p+q < r} \eta_r(p,q)}{\frac{(-1)^q \pi^{p+q} A_+^p A_-^q \sigma_+^{2p} \sigma_-^{2q}}{1+s(p\sigma_+^2+q\sigma_-^2)}} \delta\left(\nu - \frac{s}{1+s(p\sigma_+^2+q\sigma_-^2)}\right),$$

with $\eta_r(p,q) = \frac{(p+q)!}{p!q!}$ easily derived by symbolic calculation.

Note that the previous two formulas are written in the scalar case for the sake of simplicity, whereas it is straightforward to derive them in the vectorial case. It is also straightforward to derive (using symbolic calculation) for more general kernels.

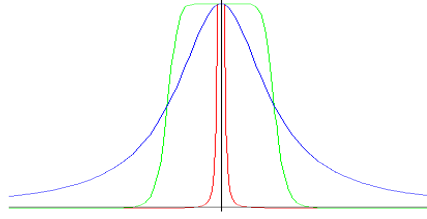


Figure 17: Three examples of rational profiles for $n = 2$ (Gaussian like, in blue) and $n = 10$ (square like, in green), and a singular profile (pointed like, in red). See text for details.

Practical implementation. From the previous results it becomes possible to design numerical routines in order to adjust at will the bump’s shape. The previous result development means that we do not have to adjust the profile in the $2D$ space but simply in the $1D$ radial profile, thanks to the Gaussian series representation. This fact very likely generalizes to non-linear profiles.

For instance, given an input $i(\nu)$ and a desired output $b_1^{\bullet}(\nu)$ the following program:

$$\min_{\theta} \int_{\nu} \left| b_1^{\bullet}(\nu) - u_{\theta, i(\nu)}^{\bullet}(\nu) \right|_{\Lambda}$$

allows to find the optimal weight parametric value θ , using e.g. the explicit formulas given previously. The choice of the measure \int_{ν} and of the metric $|\cdot|_{\Lambda}$ is application dependent.

Another application is the input control of such calculation maps: Given parameters θ , find the input $i(\nu)$ yielding a given output $b(\nu)$. The solution is straightforward in the present framework, as illustrated in Fig. 18.

Acknowledgment: Partially supported by the ANR MAPS project.

References

- [1] Frédéric Alexandre, Jérémy Fix, Axel Hutt, Nicolas Rougier, and Thierry Viéville. On practical neural field parameters adjustment. In *NeuroComp’08*, 2008.
- [2] S.-I. Amari. Dynamics of pattern formation in lateral-inhibition type neural fields. *Biological Cybernetics*, 27(2):77–87, jun 1977.
- [3] F.M. Atay and A.Hutt. Neural fields with distributed transmission speeds and long-range feedback delays. *SIAM Journal Applied Dynamical Systems*, 5(4):670–698, 2006.
- [4] P. C. Bressloff and S. E. Folias. Front bifurcations in an excitatory neural network. *SIAM J. Appl.Math.*, 65(1):131–151, 2004.

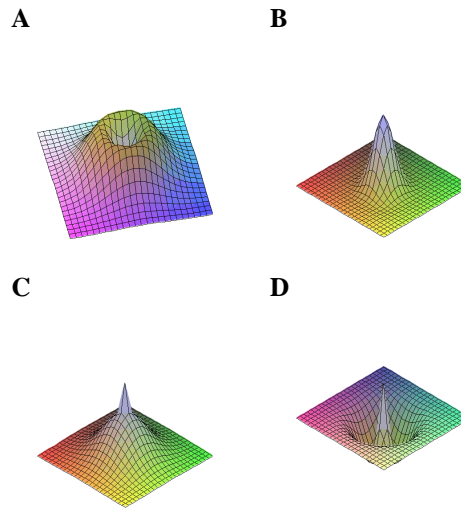


Figure 18: Four examples of input profiles yielding a Gaussian output $u(\mathbf{p}) = e^{-|\mathbf{p}|^2}$. **A:** $\theta = (1, 1, 0.2, 1)$ shown in a $[-5..5]^2$ window. **B:** $\theta = (0, 1, ., 1)$ shown in a $[-5..5]^2$ window. **C:** $\theta = (0, 0.1, ., 0.1)$ shown in a $[-20..20]^2$ window. **D:** $\theta = (1, 1, 0.02, 0.05)$ shown in a $[-20..20]^2$ window. It also shows the versatility of Gaussian series shapes.

- [5] Kurt Bryan. Elementary inversion of the laplace transform, 1999. Web publication on <http://www.rose-hulman.edu/~bryan>.
- [6] Stephen Coombes. Waves, bumps, and patterns in neural fields theories. *Biological Cybernetics*, 93(2):91–108, 2005.
- [7] P. Dayan and L. F. Abbott. *Theoretical Neuroscience : Computational and Mathematical Modeling of Neural Systems*. MIT Press, 2001.
- [8] G. B. Ermentrout and J. B. McLeod. Existence and uniqueness of travelling waves for a neural network. *Proc. Roy. Soc. Edinburgh Sect. A*, 123:461–478, 1993.
- [9] Stefanos E. Folias and Paul C. Bressloff. Breathing pulses in an excitatory neural network. *SIAM Journal on Applied Dynamical Systems*, 3(3):378–407, 2004.
- [10] F.R. Gantmacher. *Matrix Theory*. Chelsea, New-York, 1977.
- [11] P. Goldman-Rakic. Topography of cognition: parallel distributed networks in primate association cortex. *Ann. Rev. Neurosci.*, 11:137–156, 1988.
- [12] F. Grimbert. A brief overview of intracortical circuits. RR 6325, INRIA, oct 2007.
- [13] F. Grimbert. *Mesoscopic models of cortical structures*. PhD thesis, University of Nice Sophia-Antipolis, feb 2008.
- [14] F. Grimbert and O. Faugeras. Bifurcation analysis of Jansen’s neural mass model. *Neural Computation*, 18(12):3052–3068, December 2006.
- [15] Stephen Grossberg. Nonlinear neural networks: Principles, mechanisms, and architectures. *Neural Networks*, 1(1):1–97, 1988.
- [16] A. Hutt. Effects of nonlocal feedback on traveling fronts in neural fields subject to transmission delay. *Physical Review*, E 70:1–4, 2004.
- [17] A. Hutt and F. M. Atay. Spontaneous and evoked activity in extended neural populations with gamma-distributed spatial interactions and transmission delay. *Chaos, Solitons and Fractals*, 32:547–560, 2007.
- [18] T.A. Porshing. Jacobi and gauss-seidel methods for nonlinear network problems. *SIAM . Numer. Analysis*, 6(3), 1969.
- [19] O. Rochel and D. Martinez. An event-driven framework for the simulation of networks of spiking neurons. In *Proc. 11th European Symposium on Artificial Neural Networks*, pages 295–300, 2003.

-
- [20] N. Rougier. Dynamic neural field with local inhibition. *Biological Cybernetics*, 94(3):169–179, 2006.
 - [21] N. Rougier and J. Vitay. Emergence of attention within a neural population. *Neural Networks*, 19(5):573–581, 2006.
 - [22] Nikolai F. Rulkov. Modeling of spiking-bursting neural behavior using two-dimensional map. *Physical review E*, 65:041922, 2002.
 - [23] J. G. Taylor. Neural networks for consciousness. *Neural Networks*, 10(7):1207–1225, 1997.
 - [24] T. Viéville, S. Chemla, and P. Kornprobst. How do high-level specifications of the brain relate to variational approaches? *J. Physiol. Paris*, 101, 2007.
 - [25] T. Viéville and O. Rochel. One step towards an abstract view of computation in spiking neural-networks. In *International Conf. on Cognitive and Neural Systems*, 2006.
 - [26] T. Wennekers. Separation of spatio-temporal receptive fields into sums of gaussian components. *J. Computational Neuroscience*, 16(1), 2004.
 - [27] H.R. Wilson and J.D. Cowan. A mathematical theory of the functional dynamics of cortical and thalamic nervous tissue. *Biological Cybernetics*, 13(2):55–80, sep 1973.



Centre de recherche INRIA Sophia Antipolis – Méditerranée
2004, route des Lucioles - BP 93 - 06902 Sophia Antipolis Cedex (France)

Centre de recherche INRIA Bordeaux – Sud Ouest : Domaine Universitaire - 351, cours de la Libération - 33405 Talence Cedex
Centre de recherche INRIA Grenoble – Rhône-Alpes : 655, avenue de l'Europe - 38334 Montbonnot Saint-Ismier
Centre de recherche INRIA Lille – Nord Europe : Parc Scientifique de la Haute Borne - 40, avenue Halley - 59650 Villeneuve d'Ascq
Centre de recherche INRIA Nancy – Grand Est : LORIA, Technopôle de Nancy-Brabois - Campus scientifique
615, rue du Jardin Botanique - BP 101 - 54602 Villers-lès-Nancy Cedex
Centre de recherche INRIA Paris – Rocquencourt : Domaine de Voluceau - Rocquencourt - BP 105 - 78153 Le Chesnay Cedex
Centre de recherche INRIA Rennes – Bretagne Atlantique : IRISA, Campus universitaire de Beaulieu - 35042 Rennes Cedex
Centre de recherche INRIA Saclay – Île-de-France : Parc Orsay Université - ZAC des Vignes : 4, rue Jacques Monod - 91893 Orsay Cedex

Éditeur
INRIA - Domaine de Voluceau - Rocquencourt, BP 105 - 78153 Le Chesnay Cedex (France)
<http://www.inria.fr>
ISSN 0249-6399